Materials Advances

ROYAL SOCIETY OF CHEMISTRY

COMMUNICATION

View Article Online
View Journal | View Issue

Cite this: *Mater. Adv.*, 2025, 6, 9386

Received 10th September 2025,
Accepted 16th November 2025

DOI: 10.1039/d5ma01044f

rsc.li/materials-advances

Multifunctional flexible carbon aerogels based on sustainable bacterial cellulose

Seeni Meera Kamal Mohamed, *[a] Benjamin Ignatzi,[a] Rebekka Probst,[a] Beruktayet Fekadu,[b] Max Zinke,[a] Lennart Barth,[a] Marina Schwan,[a] Marion Bartsch[b] and Barbara Milow[a]

We demonstrate that a combination of bacterial cellulose (BC) and resorcinol-formaldehyde (RF) imparts flexibility to its hybrid (BC + RF) and carbon aerogels (CAs). The microstructures of the produced aerogels exhibit continuous fibers from BC over which aggregates of RF particles are formed. The flexible CAs are able to recover from repeated compressive deformation with maximum compressive strain of 80%. These flexible CAs based on sustainable BC are achieved by a simple infiltration processing route and are suitable for applications in various fields such as gas adsorption, oil absorption, catalysis, energy storage, sensors, *etc.*

Carbon aerogels (CAs) are a unique class of synthetic three-dimensional (3D) solid with exceptional ultra-low density, large surface area, high porosity, high electrical conductivity, and high environmental stability.[1–3] This has prompted the use of CAs in a wide range of applications, such as energy storage, catalysis, filtration, separation, insulation, sensors, gas storage, and microwave absorption.[4–6] However, typical CAs produced from the carbonization of organic aerogels (RF, melamine–formaldehyde, cresol–resorcinol–formaldehyde, lignin–tannin, lignin–resorcinol–formaldehyde, and others)[7–10] are fragile and brittle, which limits their applications.[1,11–13] This brittleness arises from extremely weak connections between carbon nanoparticles and fragile joints in their porous network.[14,15] In the pursuit of achieving flexibility, Schwan *et al.*[16–20] achieved for the first time flexibilization of RF aerogel (RF-A) and its CA counterpart by means of a pH-controlled route. Recently, super elastic macroscopic free-standing cobalt silicate@RF resin core–shell nanobelt aerogels were developed through *in situ* gelation.[21] Although large-scale production of flexible (f) RF-A and CA is feasible, it has several problems such as toxic and expensive precursors, complex synthesis processes and equipment.[22,23] Hence, it is essential to find a simple, sustainable, economic, and environmentally friendly route to produce f-CAs.

In order to address these challenges, bio-mass derived CAs are excellent alternatives as they are cheap, non-toxic, sustainable and easy to obtain.[24] Among several bio-masses, BC is an emerging nano-structured material produced by microorganisms through fermentation. BC has β-1,4-glycosidic linkages with a molecular formula of $(C_6H_{10}O_5)_n$, having a pure native cellulose I structure unlike other plant-based celluloses. BC is composed of highly crystalline (90%) ultrafine (5–50 nm) cellulose nanofibers (CNFs) with a high aspect ratio that is attributed to its 3D porous network structure with large surface area, high porosity, and excellent mechanical stability.[11,25,26] The direct carbonization of BC aerogels results in 3D-CAs with a disordered microstructure and poor mechanical properties because of the decomposition of BC.[22] This is because of the large shrinkage and collapse of the network structure by the capillary forces that were exerted on the pore walls during direct carbonization.[26] There have been several attempts made to produce f-CAs from BC, and few of them succeeded. BC based f-CAs were developed using different approaches like freeze-drying and dissolution-gelation followed by carbonization.[22,27–32]

In this work, we utilize the direct combination of BC and RF solution to form their hybrid in order to achieve flexibility before and after carbonization. BC samples were obtained as cubes and infiltrated with RF solution followed by gelation, solvent exchange, super-critical drying, and carbonization (Fig. S1–S3). The RF solution was prepared using the following recipe to achieve flexibilization: the molar ratios, R/C: 50, R/W: 0.008, R/F: 0.5 at pH: 5.43–5.65 at 80 °C for 1 week.[16] According to Schwan *et al.*,[18] the initial pH of the RF solution has a great influence on the flexibility of the aerogels formed with no shrinkage. The flexibility depends on the microstructure formed in this pH range and also on the super-critical drying.[18] Moreover, a well adjusted pH value promotes the

[a] *Department of Aerogels and Highly Porous Materials, Institute for Frontier Materials on Earth and in Space, German Aerospace Center (DLR), Cologne, Germany. E-mail: seenimeera.kamalmohamed@dlr.de*
[b] *Department of Digitally Integrated Microstructure and Mechanics, Institute for Frontier Materials on Earth and in Space, German Aerospace Center (DLR), Cologne, Germany*

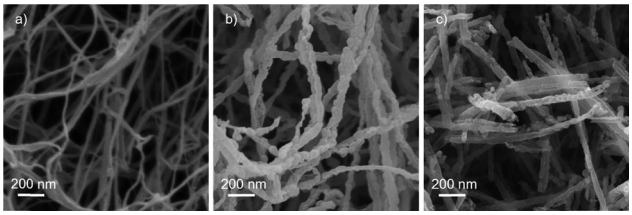

Fig. 1 SEM images of (a) BC-A, (b) BC-RF-A, and (c) BC-RF-C-A.

formation of a structure similar to the highly cross-linked and branched structure observed by Pekala and Schaefer.[33,34] The microstructure of f-RF-A produced exhibits particles forming a network structure resembling pearl chains interconnected by necks with large pores critical for their flexibility (Fig. S4a and b). The carbonization of f-RF-A leads to reduction of the diameters of the particles from sizes between 220 and 290 nm to sizes between 190 and 250 nm, with the merging of the nanoparticles closer together (Fig. S4b and d). Such microstructures have been reported for f-RF-A and f-RF-C-A by Schwan *et al.*[16–20]

BC-A showed a highly porous network structure composed of large numbers of CNFs (Fig. 1a). CNFs have a diameter of 20–50 nm and are interconnected and intertwined, respectively. The infiltration of RF polymer into the CNFs network can be clearly seen from the nanoaggregates of RF particles coating the CNFs in BC-RF-A (Fig. 1b). RF coated CNFs have diameters of 70–85 nm. After carbonization at 1000 °C, the microstructure of BC-RF-A was retained with a slight reduction of the size of the coated fibres to 40–50 nm (Fig. 1c).

The BC-RF-C-A is an ultralight aerogel as illustrated in Fig S5. An overview of skeletal and bulk density and porosity of the different aerogels is provided in Table 1.

The pristine BC-A has the highest porosity with the lowest bulk density. RF infiltration reduced the porosity and increased the bulk density as expected while the skeletal density did not change significantly. The subsequent carbonization resulted in an increase of porosity and reduction of bulk density but also an increase of skeletal density. The effect of carbonization was similar for f-RF-A. A similar trend has been reported by Xu *et al.*[32] for BC-lignin-resorcinol-formaldehyde-based CAs.

To evaluate surface area and porosity, N_2 sorption analyses were performed. An overview of the determined data is given in Table 2, the isotherms are displayed in Fig. 2a and Fig. S5, and pore size distributions obtained by Barret–Joyner–Halenda (BJH) and density functional theory (DFT) are provided in Fig. S8.

Table 1 Densities and porosities of different aerogels

Sample codes	Skeletal density (ρ_s) g cm^{-3}	Bulk density (ρ_b) g cm^{-3}	Porosity (%) $(1 - (\rho_b/\rho_s)) \times 100$
BC-A	1.78 ± 0.06	0.009 ± 0.00	99.5 ± 0.01
BC-RF-A	1.75 ± 0.01	0.056 ± 0.00	96.7 ± 0.01
BC-RF-C-A	2.12 ± 0.08	0.023 ± 0.00	98.9 ± 0.01
f-RF-A	1.44 ± 0.01	0.101 ± 0.00	92.9 ± 0.01
f-RF-C-A	2.09 ± 0.02	0.074 ± 0.00	96.4 ± 0.01

BC-A exhibits a type IV isotherm with H3 loop because the pore network contains macropores that are not completely filled by pore condensate (Fig. 2a).[35] BC-A has a total specific surface area (SSA_{total}) of 249 ± 0.60 m^2 g^{-1} with a total pore volume ($V_{p,des}$) of 0.59 cm^3 g^{-1}. The infiltration of RF nanoaggregates into the nanofibrillar network of BC (Fig. 1b) decreased the total pore volume to 0.38 cm^3 g^{-1}, which indicates that not only nanofibers are coated with RF but also mesopores are filled with RF nanoaggregates. BC-RF-A exhibits a reversible type II isotherm with a sharp knee, characteristic of physisorption of gases on nonporous or macroporous adsorbents (Fig. 2a).[36] Upon carbonization, BC-RF-C-A has a type I(a) isotherm provided by microporous solids, which is confirmed by a steep increase of N_2 uptake at low p/p^0 value with a narrow micropore size distribution (pore width of ≤1 nm, displayed in Fig. S7) with small contribution from type IV behaviour (Fig. 2a). The overall structure of the isotherm is retained in comparison to BC-A and BC-RF-A with an additional gas uptake at very low relative pressures (0–0.1 p/p^0) (Fig. 2a). N_2 gas uptake is indicated by a plateau in the relative pressure range between $0.1 < p/p^0 < 0.8$ and the appearance of hysteresis with the rapid increase of gas uptake at high p/p^0 (> 0.8). The SSA_{total} of BC-RF-C-A is substantially increased to 1527 ± 2.99 m^2 g^{-1} with an external surface area of 1023 m^2 g^{-1} and a micropore area of 504 m^2 g^{-1}. The total pore volume at a relative pressure of 0.995 p/p^0 is 1.74 cm^3 g^{-1} with a micropore volume ($V_{p,micro}$) of 0.22 cm^3 g^{-1}. Overall, mesopores account for 65–70% of the total specific surface area as provided by the SSA_{meso}/SSA_{total} values (Table 2). The increased surface area and the development of micropores are because of the removal of water and organics from the nanocellulose and RF structure as evidenced by thermogravimetric analyses (TGA) shown in Fig. S9.

The BJH desorption average pore widths ($D_{p,des}$) of BC-A and BC-RF-A are found to be 8.4 and 6.9 nm, respectively. They exhibit a narrow pore size distribution between 2 and 100 nm (Fig. S8). The steeper slope of the adsorption curves at high pressure range compared to that in intermediate and low-pressure ranges is associated to capillary coalescence in large mesopores.[37] The existence of micropores in BC-RF-C-A and f-RF-C-A is confirmed by the pore size distribution. The two different CAs show micropore widths of ∼ 0.6 and ∼ 1.3 nm, respectively (Fig. S8). The predominance of micropores in CAs is inherited from the pyrolysis of their pristine aerogels.

The investigation of CO_2 adsorption of CAs was performed at 273 and 298 K in the pressure range of 0–1.1 bar. They exhibit a type I isotherm characteristic of microporous materials,[38] which is presented in Fig. 2b and Fig. S10. The slope of the adsorption isotherm is reduced due to the increase in temperature as adsorption is an exothermic process. The CO_2 adsorption capacity of two different CAs at partial pressure of CO_2 and atmospheric pressure is presented in Table 3.

The CO_2 adsorbed at 273 K reached 4.30 and 1.53 mmol g^{-1} at 1 and 0.1 bar, respectively, whereas at 298 K it is only 2.68 and 0.76 mmol g^{-1} at 1 and 0.1 bar, respectively. The adsorption is more of a monolayer at higher temperatures whereas it is multilayer at lower temperatures.[39] This means that the

Table 2 N_2 physisorption data of different aerogels

Sample codes	SSA_{total} ($m^2\ g^{-1}$)	BET C constant	SSA_{meso} ($m^2\ g^{-1}$)	SSA_{micro} ($m^2\ g^{-1}$)	SSA_{meso}/SSA_{total} (%)	SSA_{micro}/SSA_{total} (%)	$V_{p,des}$ ($cm^3\ g^{-1}$)	$V_{p,micro}$ ($cm^3\ g^{-1}$)	$D_{p,des}$ (nm)
BC-A	249 ± 0.60	21	—	—	—	—	0.59	—	8.4
BC-RF-A	218 ± 0.61	22	—	—	—	—	0.38	—	6.9
BC-RF-C-A	1527 ± 2.99	204	1023	504	66.9	33.1	1.74	0.22	7.4
f-RF-A	78 ± 0.53	7.7	—	—	—	—	0.09	—	4.8
f-RF-C-A	1191 ± 0.54	1529	429	762	36.1	63.9	0.74	0.31	4.8

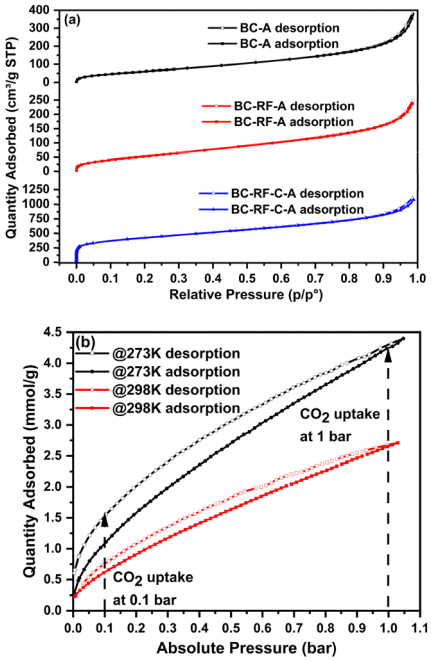

Fig. 2 (a) N_2 and (b) CO_2 sorption isotherms of the prepared different aerogels. Expanded low and high p/p^0 regions of the N_2 sorption isotherms are presented in Fig. S6.

Table 3 CO_2 adsorption properties of different flexible carbon aerogels

	CO_2 adsorption capacity (mmol g^{-1})@T (K)			
Sample codes	1 bar	0.1 bar	1 bar	0.1 bar
BC-RF-C-A	4.30@273	1.53@273	2.68@298	0.76@298
f-RF-C-A	4.78@273	1.80@273	3.72@298	1.50@298

adsorbed CO_2 molecules gain more kinetic energy at higher temperature, which makes it easier for the molecules to detach from the surface and desorb.

The structural and functional properties of the produced aerogels were investigated using FT-IR, XRD, and Raman spectroscopy. Fig. S11 depicts FT-IR spectra of different aerogels. The characteristic functional groups of BC-A result in five major bands, namely O–H stretching, C–H stretching, –OH bending, H–C–H bending, and C–H bending at 3350, 2916, 1427, 1050, and 870 cm^{-1}, respectively.[40] Resorcinol and formaldehyde molecules undergo gelation in the presence of a BC hydrogel network. As the gelation proceeds, resorcinol and formaldehyde react together in the presence of sodium carbonate at 80 °C and form a hydroxymethyl derivative, which leads to the formation of methylene and a methylene ether bridged gel network. FT-IR spectra of BC-RF-A show few additional peaks at 1450 and 1299 cm^{-1} assigned to $-CH_2$ bending and C–O stretching, respectively. The C–O–C linkage stretching exhibits two distinct peaks at 1210 and 1070 cm^{-1}.[41] The appearance of these new peaks confirmed the formation of RF network over the CNFs. Furthermore, carbonization leads to the disappearance of major organic functional groups and exhibits only peaks related to the carbon network such as C=C stretching, H–C–H bending, and C–H bending at 1650, 1050, and 870 cm^{-1}, respectively (Fig. S11).

The XRD pattern of BC-A shows the cellulose-I structure, and its characteristic peaks appeared at 2θ of 15.18°, 17.74°, and 23.59°, related to (1 0 0), (0 1 0), and (1 1 0) planes, respectively. This confirms that cellulose I_α is the type of cellulose constructing the aerogel.[42] f-RF-A exhibits a typical prominent (0 0 2) peak (broader) between 10 and 40° and a non-prominent (1 0 0) peak at 40° over an amorphous background (Fig. S12).[43] The XRD pattern of BC-RF-A turned into a blend of the diffraction pattern of BC-A and f-RF-A, and sharp crystalline peaks of BC-A appeared over the broad amorphous diffraction pattern of f-RF-A (Fig. 3a and Fig. S12). Upon carbonization, BC-RF-C-A displayed a broad diffraction peak at 24 and 43° corresponding to the (0 0 2) and (1 0 0) planes of the graphitic lattice planes (f-RF-C-A has a similar diffraction pattern, Fig. S12).[27,44]

Fig. 3b represents the Raman spectra of the amorphous and crystalline regions of different CAs. The spectra exhibit two bands, characteristic of aromatic 6-membered rings at around 1340 and 1590 cm^{-1} responsible for the D- and G-bands, respectively.[45] The high intensity D-band (A_{1g} symmetry, disordered carbon with structural defects) at around 1340 cm^{-1} is associated with the breathing mode of sp^2 carbon present in the 6-membered aromatic rings with defects. The low intensity G-band (E_{2g} symmetry) at around 1590 cm^{-1} is caused by the bond stretching motion of the sp^2 hybridized carbon atoms in the graphitic structure. The I_D/I_G ratio for both types of CAs is calculated to be 1.35 ± 0.01. Higher I_D/I_G ratios are reported for disordered carbon materials like amorphous carbon with high concentration of defects.[40] It is clearly evident from the high I_D/I_G ratio that both CAs have defects, disorder, and disruption in the 2D hexagonal lattice.[46] These defects contribute to the micropore volume and determine the active sites for gas and ion adsorption.[47]

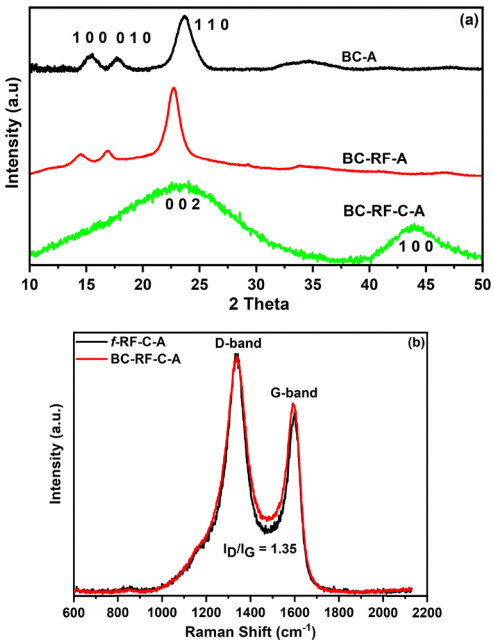

Fig. 3 XRD (a) and Raman (b) spectra of the prepared different aerogels.

The decoration of CNFs by the nanoaggregates of RF nanoparticles imparts high flexibility to the BC-RF-C-A, as has been demonstrated by the cyclic compression tests with a maximum compressive strain of 80% for 100 cycles, as displayed in Fig. 4. With increasing number of cycles, the recovery of the material is reduced, but it maintained its structural integrity as can be observed in Video S1. SEM images of BC-RF-C-A in its pristine state, after 1 cycle and 100 cycles, respectively, did not show any evidence of damage, comparing Fig. 1c and Fig. S13.

The surface wettability of BC-RF-C-A was determined by water contact angle (WCA) measurements. The surface of the aerogel exhibited hydrophobicity with a WCA of 130.7° (Fig. S14, Video S2 and Table S1). However, the cyclohexane droplet was immediately absorbed, and the cyclohexane contact angle was found to be 0° (Fig. S15). This clearly evidences the high hydrophobic and super oleophilic nature of the flexible BC-RF-C-A.

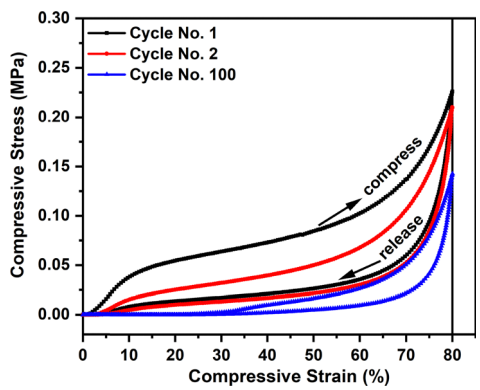

Fig. 4 Stress–strain curves of cyclic strain-controlled compressive tests on a BC-RF-C-A with a maximum strain of 80%.

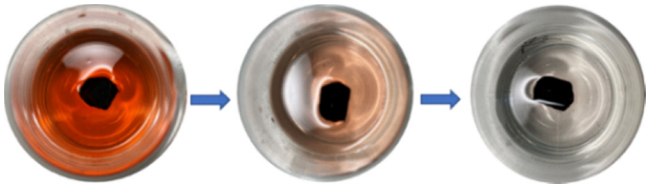

Fig. 5 Oil absorption studies of the flexible BC-RF-C-A in artificial sea-water (3.5% NaCl) mixed with cyclohexane dyed with Sudan III.

Owing to low-density, high porosity, and hydrophobicity, the ultralight flexible BC-RF-C-A is a good candidate for the absorption of oil and other organic pollutants. The oil absorption capacity was tested using artificial sea water (3.5% NaCl) mixed with cyclohexane, dyed with Sudan III dye (Fig. S16) and placing a piece of BC-RF-C-A on the surface of the oil–water mixture. It exhibits an oil absorption capacity of 40–50 times its original weight (Fig. 5 and Video S3). The oil absorption capacity in % weight gain is found to be around 3700% for cyclohexane.

Furthermore, flexible BC-RF-C-A exhibits fire resistance properties when exposed to the flame of a butane/propane mix gas burner (in air) and sustained for about 1 minute (Video S4).

In conclusion, we developed a multi-functional flexible carbon aerogel from sustainable BC through simple infiltration of RF followed by gelation, drying, and carbonization. The flexibility of BC based CAs arises from the combination of interconnected nanofibers from BC and particles forming a pearl like network structure, which are interconnected by necks with large porosity from RF.

Author contributions

SMKM: conceptualization, methodology, investigation, validation, writing – original draft, writing – review and editing, and visualization; BI: methodology and validation; RP: methodology and validation; BF: methodology and validation; MZ: methodology and validation; LB: methodology and validation; MS: project administration, writing – review and editing; MB: methodology, validation; writing – original draft, writing – review and editing, and visualization; BM: project administration, writing – review and editing, and supervision.

Conflicts of interest

The authors declare no conflicts of interest.

Data availability

The data supporting this article have been included as part of the supplementary information (SI). Supplementary information: experiments, materials and methods, SEM, FT-IR, TGA, XRD, oil absorption, flame retardancy, contact angle, N_2 and CO_2 adsorption isotherm, pore size distribution, tables and videos. See DOI: **https://doi.org/10.1039/d5ma01044f**.

Acknowledgements

This work was performed in the context of a project ''FisBatt''. The funding by the DLR Program Directory Energy is gratefully acknowledged. We wish to thank Dr Pascal Vöpel for the realization of the graphical abstract. We also would like to acknowledge the colleagues, Mr Torben Reuter, Ms Lana Möltgen and Mr Alexander Francke for their support in Raman, TGA and XRD measurements.

Notes and references

1 M. Salihovic, N. Hüsing, J. Bernardi, V. Presser and M. S. Elsaesser, *RSC Adv.*, 2018, **8**, 27326–27331.
2 M. A. Worsley, M. Stadermann, Y. M. Wang, J. H. Satcher Jr and T. F. Baumann, *Chem. Commun.*, 2010, **46**, 9253–9255.
3 S. Li, D. Hou, Y. Cui, S. Jia, G. Lan, W. Sun, G. Li, X. Li and W. Feng, *Carbon*, 2024, **218**, 118669.
4 N. Liu, J. Shen and D. Liu, *Microporous Mesoporous Mater.*, 2013, **167**, 176.
5 L. Zhuang, D. Lu, J. Zhang, P. Guo, L. Su, Y. Qin, P. Zhang, L. Xu, M. Niu, K. Peng and H. Wang, *Nat. Commun.*, 2023, **14**, 3178.
6 L. Hu, R. He, H. Lei and D. Fang, *Int. J. Thermophys.*, 2019, **40**, 39.
7 J. Biener, M. Stadermann, M. Suss, M. A. Worsley, M. M. Biener, K. A. Rose and T. F. Baumann, *Energy Environ. Sci.*, 2011, **4**, 656.
8 S. Chandrasekaran, P. G. Campbell, T. F. Baumann and M. A. Worsley, *J. Mater. Res.*, 2017, **32**, 4166–4185.
9 D.-W. Park, N. A. Cañas, M. Schwan, B. Milow, L. Ratke and K. A. Friedrich, *Curr. Appl. Phys.*, 2016, **16**, 658–664.
10 R. W. Pekala, *US Pat.*, PPN: US 7-199404, 1989.
11 Z.-Y. Wu, H.-W. Liang, L.-F. Chen, B.-C. Hu and S.-H. Yu, *Acc. Chem. Res.*, 2016, **49**, 96–105.
12 H. Zhang, J. Feng, L. Li, Y. Jiang and J. Feng, *RSC Adv.*, 2022, **12**, 13783–13791.
13 J. Feng, C. Zhang and J. Feng, *Mater. Lett.*, 2012, **67**, 266–268.
14 K. Wu, Q. Zhou, J. Cao, Z. Qian, B. Niu and D. Long, *J. Colloid Interface Sci.*, 2022, **609**, 667–675.
15 F. Guo, Y. Jiang, Z. Xu, Y. Xiao, B. Fang, Y. Liu, W. Gao, P. Zhao, H. Wang and C. Gao, *Nat. Commun.*, 2018, **9**, 881.
16 M. Schwan and L. Ratke, *J. Mater. Chem. A*, 2013, **1**, 13462–13468.
17 R. Tannert, M. Schwan and L. Ratke, *J. Supercrit. Fluids*, 2015, **106**, 57–61.
18 M. Schwan, R. Tannert and L. Ratke, *J. Supercrit. Fluids*, 2016, **107**, 201–208.
19 M. Schwan, M. Naikade, D. Raabe and L. Ratke, *J. Mater. Sci.*, 2015, **50**, 5482–5493.
20 M. Schwan and L. Ratke, *C*, 2016, **2**, 22.
21 F. Li, J. Song, Y. Niu, H. Zhang, M. Niederberger and W. Cheng, *Small*, 2023, **19**, 2302724.
22 B. Wang, X. Yin, R. Cheng, J. Li, G. Ying and K. Chen, *Carbon*, 2022, **199**, 318–328.
23 Z.-Y. Wu, C. Li, H.-W. Liang, J.-F. Chen and S.-H. Yu, *Angew. Chem., Int. Ed.*, 2013, **52**, 2925–2929.
24 D. Yang, P. Xu, C. Tian, S. Li, T. Xing, Z. Li, X. Wang and P. Dai, *Molecules*, 2023, **28**, 6377.
25 Y. Wan, Z. Yang, G. Xiong and H. Luo, *J. Mater. Chem. A*, 2015, **3**, 15386.
26 M. Panahi-Sarmad, N. Alikarami, T. Guo, M. Haji, F. Jiang and O. J. Rojas, *Small*, 2024, **20**, 2403583.
27 Z. Cheng, J. Li, B. Wang, J. Zeng, J. Xu, W. Gao, S. Zhu, F. Hu, J. Dong and K. Chen, *ACS Appl. Bio Mater.*, 2020, **3**, 7483–7491.
28 L. Wang, C. Schutz, G. Salazar-Alvarez and M.-M. Titirici, *RSC Adv.*, 2014, **4**, 17549–17554.
29 B. Wang, X. Li, B. Luo, J. Yang, X. Wang, Q. Song, S. Chen and L. Zhi, *Small*, 2013, **9**(14), 2399–2404.
30 H.-W. Liang, Q.-F. Guan, Zhu-Zhu, L.-T. Song, H.-B. Yao, X. Lei and S.-H. Yu, *NPG Asia Mater.*, 2012, **4**, e19.
31 C. Li, Y.-W. Ding, B.-C. Hu, Z.-Y. Wu, H.-L. Gao, H.-W. Liang, J.-F. Chen and S.-H. Yu, *Adv. Mater.*, 2020, **32**, 1904331.
32 X. Xu, J. Zhou, D. H. Nagaraju, L. Jiang, V. R. Marinov, G. Lubineau, H. N. Alshareef and M. Oh, *Adv. Funct. Mater.*, 2015, **25**, 3193–3202.
33 R. Pekala and D. W. Schaefer, *Macromolecules*, 1993, **26**, 5487–5493.
34 D. W. Schaefer, R. Pekala and G. Beaucage, *J. Non-Cryst. Solids*, 1995, **186**, 159–167.
35 M. Thommes, K. Kaneko, A. V. Neimark, J. P. Olivier, F. Rodriguez-Reinoso, J. Rouquerol and K. S. W. Sing, *Pure Appl. Chem.*, 2015, **87**, 1051–1069.
36 B. Liu, X. Ma, D. Wei, Y. Yang, Z. Zeng and L. Li, *Carbon*, 2022, **192**, 41–49.
37 Y. Huang, H. Yang, Y. Yu, H. Li, H. Li, J. Bai, F. Shi and J. Liu, *J. Environ. Chem. Eng.*, 2023, **11**, 110403.
38 J. Gong, F. Tong, C. Zhang, M. S. Nobandegani, L. Yu and L. Zhang, *Microporous Mesoporous Mater.*, 2022, **331**, 111664.
39 H. Jedli, S. M. Bouzgarrou, R. Hassani, E. Sabi and K. Slimi, *J. Therm. Anal. Calorim.*, 2025, **150**, 7439–7449.
40 L. Wannasen, N. Chanlek, W. Mongkolthanaruk, S. Daengsakul and S. Pinitsoontorn, *Mater. Sci. Energy Technol.*, 2025, **8**, 13–23.
41 M. Mohsenpour, S. Motahari, F. Tajabadi and M. Najafi, *RSC Adv.*, 2020, **10**, 41780–41790.
42 H. Sai, R. Fu, L. Xing, J. Xiang, Z. Li, F. Li and T. Zhang, *ACS Appl. Mater. Interfaces*, 2015, **7**, 7373–7381.
43 S. Kamal Mohamed, C. Heinrich and B. Milow, *Polymers*, 2021, **13**, 2409.
44 S. Singh, A. Bhatnagar, V. Dixit, V. Shukla, M. A. Shaz, A. S. K. Sinha, O. N. Srivastava and V. Sekkar, *Int. J. Hydrogen Energy*, 2016, **41**, 3561–3570.
45 M. Nojabaee, B. Sievert, M. Schwan, J. Schettler, F. Warth, N. Wagner, B. Milow and K. A. Friedrich, *J. Mater. Chem. A*, 2021, **9**, 6508–6519.
46 A. Dychalska, P. Popielarski, W. Frankow, K. Fabisiak, K. Paprocki and M. Szybowicz, *Mater. Sci.-Poland*, 2015, **33**, 1–7.
47 A. V. Patil, S. R. Gurav, R. G. Sonkawade and R. S. Vhatkar, *Energy*, 2024, **307**, 132471.